












## TIME Commissioning Observations: II. On-sky Characterization and the 2D Map Data Processing Pipeline

BENJAMIN J. VAUGHAN <sup>1</sup>, ABIGAIL T. CRITES <sup>1,2,3</sup>, DONGWOO T. CHUNG <sup>2</sup>, RYAN P. KEENAN,<sup>4</sup> JAMES J. BOCK,<sup>3,5</sup>  
CHARLES M. BRADFORD,<sup>3,5</sup> VICTORIA L. BUTLER <sup>1</sup>, TZU-CHING CHANG,<sup>5</sup> YUN-TING CHENG,<sup>3,5</sup> AUDREY DUNN <sup>6</sup>,  
NICHOLAS EMERSON,<sup>7</sup> CLIFFORD FREZ,<sup>5</sup> JONATHON HUNACEK,<sup>5</sup> CHAO-TE LI,<sup>8</sup> IAN N. LOWE <sup>7</sup>, KING LAU,<sup>3</sup>  
DANIEL P. MARRONE,<sup>7</sup> EVAN C. MAYER <sup>7</sup>, SOPHIE M. McATEE <sup>1</sup>, DANG PHAM,<sup>9,10</sup> SHWETHA PRAKASH <sup>1</sup>,  
GUOCHAO SUN,<sup>11</sup> ISAAC TRUMPER,<sup>7</sup> ANTHONY D. TURNER,<sup>5</sup> TA-SHUN WEI,<sup>8</sup> SELINA F. YANG <sup>1</sup>  
AND MICHAEL ZEMCOV <sup>6,5</sup>  
THE TIME COLLABORATION

<sup>1</sup>*Department of Physics, Cornell University, Ithaca NY 14853, USA*

<sup>2</sup>*Department of Astronomy, Cornell University, Ithaca NY 14853, USA*

<sup>3</sup>*Department of Physics, California Institute of Technology, Pasadena, California 91125, USA*

<sup>4</sup>*Max-Planck-Institut für Astronomie, Königstuhl 17, D-69117 Heidelberg, Germany*

<sup>5</sup>*Jet Propulsion Laboratory, California Institute of Technology, Pasadena, California 91109, USA*

<sup>6</sup>*Rochester Institute of Technology, Rochester, NY, 14623, USA*

<sup>7</sup>*Department of Astronomy and Steward Observatory, University of Arizona, 933 N Cherry Avenue, Tucson, AZ 85721, USA*

<sup>8</sup>*Institute of Astronomy and Astrophysics, Academia Sinica, Taipei, Taiwan*

<sup>9</sup>*JILA and Department of Astrophysical and Planetary Sciences, CU Boulder, Boulder, CO 80309, USA*

<sup>10</sup>*David A. Dunlap Department of Astronomy and Astrophysics, University of Toronto, 50 St. George Street, Toronto, ON M5S 3H4, Canada*

<sup>11</sup>*CIERA and Department of Physics and Astronomy, Northwestern University, 1800 Sherman Avenue, Evanston, IL 60201, USA*

### ABSTRACT

The Tomographic Ionized-carbon Mapping Experiment (TIME) is a line intensity mapping (LIM) instrument that is designed to observe the power spectrum of the [CII] 158  $\mu\text{m}$  emission line during the Epoch of Reionization. TIME completed a commissioning run in 2022 at the Arizona Radio Observatory onboard the 12-M Radio Telescope at Kitt Peak, where it observed galactic sources for the first time. In this paper we report on an analysis of observations of the Orion Molecular Cloud (OMC) and G49.5 (a local HII region). The OMC observations were taken at least once a day to assess the stability of the instrument and demonstrate its on-sky performance. We describe a spectral image processing pipeline to make calibrated maps of raster scans of these sources, incorporating planet observations for gain calibration. We show with G49.5 that, when compared to the Bolocam Galactic Plane Survey, we are able to achieve a  $< 3\%$  calibration difference. Based on the outcomes from this commissioning phase of TIME, we have demonstrated preliminary performance, and identified sources of improvement necessary for pursuing a LIM measurement.

### 1. INTRODUCTION

We have deployed the Tomographic Ionized-carbon Mapping Experiment (TIME) at the Arizona Radio Observatory 12 Meter (ARO-12M) telescope and in this paper present on-sky characterization measurements during the 2022 commissioning. TIME (A. T. Crites et al. 2014) is an imaging spectrometer that operates in a frequency range of 183–326 GHz with a spectral resolution of  $R \sim 100$ . TIME’s primary science cases are: observations of the [CII] 158  $\mu\text{m}$  forbidden transition line emitted during the epoch of reionization over redshifts

$6 \lesssim z \lesssim 9$ ; and observations of CO rotational lines during cosmic noon ( $1 \lesssim z \lesssim 2$ ). These measurements allow us to probe the history of star formation rate during these two epochs; The [CII] measurements provide direct access to the luminosity of photo-disassociation regions, and CO measurements give an estimation of the molecular hydrogen gas content (G. Sun et al. 2021; E. Kovetz et al. 2019). With TIME, we access this information by producing a set of tomographic intensity maps, and computing the 3-D power spectrum of these emission lines. The design requirements needed to achieve this

goal, low spectral resolution over a wide spectral range, also permit the production of a wealth of information about molecular clouds, planetary nebulae, and other forms of spatially extended mm-wavelength emission.

To prepare for LIM measurements, TIME underwent a commissioning season culminating in 11 days of on-sky observations during the winter of 2022. A variety of objects were studied including local molecular clouds (this work), the galactic center (S. F. Yang et al. 2026), planets, and quasars. These observations are split into two categories: 1-D line scans largely designed to characterize the noise in the instrument, and 2-D rasters. Here we focus on the 2-D raster observations of planets and molecular clouds that allow us to characterize the full on-sky performance of TIME. In particular, we produce calibrated spectral images of the Orion Molecular Cloud (OMC) complex (J. Bally 2008) which was observed at least once a day throughout the whole commissioning, and G49.5, a local HII region (J. M. Carpenter & D. B. Sanders 1998). The OMC complex and G49.5 are two of the brightest radio sources in the sky with significant CO (2-1) emission (S. Fujita et al. 2021; B. A. Wilson et al. 2005), making them well-studied and suited for understanding the performance of TIME.

This paper is structured as follows. In §2 we describe the status of the TIME focal plane, the observing strategy and how the raw data is packaged. In §3, the process of converting these raw data to on-sky maps and calibrating observations to physical units is described. In §4, we process one G49.5 Observation and compare its flux against the Bolocam Galactic Plane Survey (J. E. Aguirre et al. (2011), BGPS). In §5, we process observations of the Orion Molecular Cloud complex (OMC), and in §6, we discuss the implications of these results for future TIME surveys.

## 2. THE STATE OF THE INSTRUMENT

TIME is comprised of two grating spectrometer banks that each have sixteen feedhorns arranged in a line (C.-T. Li et al. 2018). Light that enters the TIME cryostat is split into two beams of different polarizations, and each beam is sent to a different spectrometer bank. The photo-detectors utilized are transition edge sensor (TES) bolometers (V. L. Butler et al. 2026; J. Hunacek et al. 2018; V. L. Butler et al. 2024) that are readout via standard multichannel electronics (MCE; E. S. Battistelli et al. 2008). During observations, the TIME cryostat is mounted in the receiver cabin of the ARO-12M telescope. TIME is then optically coupled to the telescope through a set of aluminum mirrors (E. C. Mayer et al. 2025). A subset of these mirrors, henceforth referred to as the K-mirror, are motorized to correct for

image rotations that are induced by the changing parallactic angle throughout an observation.

### 2.1. Status of the TIME Focal Plane

During commissioning, we did not have a fully populated focal plane as we were still prototyping our detectors, and only one spectrometer bank was present in the instrument. The focal plane is split into 24 detector sub-arrays (see V. L. Butler et al. (2024) for a full description), which consist of two physically different varieties, low frequency (183-230 GHz) and high frequency (230-323 GHz). Each sub-array was produced on the same wafer, and then further diced into separate detector modules. These modules are then mounted onto the back-side of the diffraction gratings (C.-T. Li et al. 2018); during this run, unpopulated modules were used to block stray light from portions of the focal plane with missing detectors. Despite the prototype nature of the detectors used in this deployment, we were able to populate the focal plane so as to have almost full spectral coverage in this set of observations.

### 2.2. Observing Strategy and Raw Data

Over the course of TIME’s 11-day commissioning we made over 300 observations across a total of  $\sim 203$  hours. Throughout this session, the observing strategy was iterated and improved. We discuss now the generic observing strategy for a TIME observation, which is a simple 2-D raster for extended radio sources. In this scheme, we hold one coordinate constant (e.g. declination) and scan the instrument across the other (e.g. right ascension). We then step to the next constant-coordinate grid point, scan in the “fast” coordinate, and repeat this process until we have mapped out a 2-D grid on the sky.

There are a few factors to keep in mind for optimizing scan parameters. One example is the impact of scan traversal time on the baseline drifts we see from  $1/f$  noise present in the data. Another is the detector physics for the TES bolometers used in TIME. These detectors have a time constant (see chapter 5.2 of J. Hunacek (2020) for a full description) which causes the beam pattern to be smeared out along the scan direction. Clear examples of this effect are shown in Figure 2.

### 2.3. The Effect of Atmosphere on Our Observations

The ARO-12M monitors the 225 GHz atmospheric opacity,  $\tau_{225GHz}$ , using a tipper, however in Winter 2022 the tipper was not functioning. Instead, we use estimates of the atmospheric opacity and precipitable water vapor (PWV) using from the ARO’s forecast. These

## SPACETIME Spectral Image Processing Pipeline

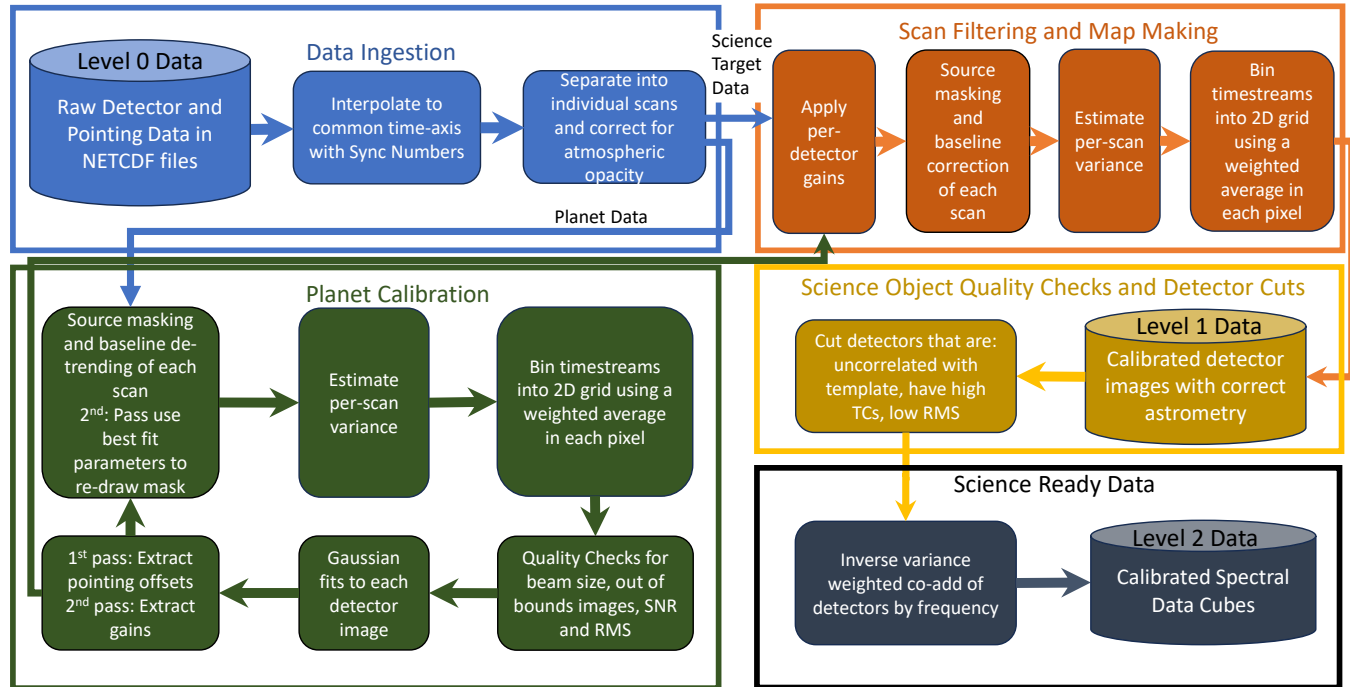


**Figure 1.** A flow chart describing the map-making process. We start with a planet observation; it is first processed using a peak finding algorithm to mask the planet signal during baseline de-trending. Next, Gaussian beams are fit to these maps and are used to estimate the feedhorn pointing offsets, and refine the mask position. The planet data is then reprocessed with this new mask, Gaussian beams are re-fit to this data, and the gains are extracted. The gains and feedhorn offsets are then applied to the science target data, which is then processed into calibrated spectral images.

forecasts are generated using the *AM* software [S. Paine \(2022\)](#) and the NOAA GFS forecast for atmosphere over Kitt Peak at the time of observation. We extrapolate  $\tau_{225GHz}$  to  $\tau_\nu$  for the nominal frequency of each detector again using *AM*, assuming a standard mid-latitude atmosphere and an elevation of 1900 m.

Since, the opacity at Kitt Peak is relatively high ( $\tau_{225} \sim 0.1$  at zenith in the top 10% of conditions) atmosphere is the most significant systematic present in our data. It has two components: atmospheric attenuation, which weakens astrophysical signals; and atmospheric emission, which generates a time-varying source of photons with a  $1/f$  spectrum whose characteristics are dependent on meteorological conditions and observed frequency ([J. Sayers et al. 2010](#)).

### 2.4. OMC and G49.5 Observations

OMC was observed at least once a day during TIME commissioning operations for a total of 20 observations, and over a wide range of scan parameters. In addition to this, the detectors were tuned three times throughout these operations giving us three different calibrations. This makes OMC a good testbed for understanding the stability of our instrument. To give a frame

of reference for the absolute calibration between these different phases of TIME’s commissioning we also took observations of G49.5 at high elevation and during good weather, which are compared to BGPS observations to assess the accuracy and precision of our calibration in Section 4.

The raw data for TIME observations comes in the form of time-ordered-data (TOD) for the telescope’s pointing, operational flags (e.g. whether or not the telescope is in a turnaround zone), and each detector’s flux measurement. The telescope signals are then interpolated onto the detector timestreams. We use the operational data to sort the pointing and detector TODs into individual raster scans and process those into maps using a software pipeline that we call *SPACETIME* (Sky Pointing and Amplitude Calibration Estimator for TIME). This pipeline implements the procedure outlined in Figure 1 and the following section.

### 3. MAP MAKING AND CALIBRATION

A critical step towards analyzing these data is their projection into an image. As described in the preceding section, and outlined in Figure 1, we start with a set of TOD that has been sorted by raster scan. Then we

**Table 1.** Sensitivity and Mapping Speed Estimates

Observation ID	Zenith Angle [deg]	Spatial Resolution [arcsec]	$\tau_{225}$
1644113101	42.8	18	$14.0^{+0.1}_{-0.1} \times 10^{-2}$
1644116132	38.4	18	$14.2^{+0.1}_{-0.1} \times 10^{-2}$
1644037749	43.4	18	$8.22^{+0.06}_{-0.06} \times 10^{-2}$
1644044143	59.2	18	$7.70^{+0.8}_{-0.8} \times 10^{-2}$
1643934288	60.1	7.2	$13.2^{+0.1}_{-0.1} \times 10^{-2}$
1644027210	42.1	18	$7.8^{+0.1}_{-0.1} \times 10^{-2}$
1644034635	38.6	18	$8.2^{+0.1}_{-0.1} \times 10^{-2}$
1644030361	38.0	18	$8.0^{+0.1}_{-0.1} \times 10^{-2}$
1643680397 <sup>†</sup>	43.4	3.6	$14^{+1}_{-1} \times 10^{-2}$
1643687384 <sup>†</sup>	39.1	3.6	$18^{+2}_{-2} \times 10^{-2}$
1643696552 <sup>†</sup>	51.4	3.6	$19^{+1}_{-1} \times 10^{-2}$
1643698876	56.8	3.6	$20.3^{+0.3}_{-0.3} \times 10^{-2}$
1643700759	62.8	3.6	$20.0^{+0.4}_{-0.4} \times 10^{-2}$
1644002746*	29.9	3.6	$8.55^{+0.05}_{-0.05} \times 10^{-2}$

NOTE—A table of observations used in this analysis given demarcated by their observation ID. The zenith angle and the  $\tau_{225}$  measurement that are used to correct for opacity are shown in columns 1 and 3 respectively, and the spatial resolution of each observation is shown in column 2. We use only the observations noted by a <sup>†</sup> symbol in Figure 4, as they have the highest spatial resolution available while minimizing the effect of bad weather. We also limit this analysis to 13 out of the 20 OMC observations as some observations were intentionally taken slightly out of focus. The starred observation is the G49.5 measurement used in §4. Notably, the observing conditions during this measurement are in the top 10% of weather and at a low zenith angle.

correct for atmospheric attenuation;

$$\gamma = \exp(-\tau(\nu) \sec(z)). \quad (1)$$

Above,  $\tau(\nu)$  is the atmospheric opacity as a function of frequency and  $z$  is the zenith angle. Then we mask the source and subtract a fitted polynomial to remove baseline drifts in the detector timestreams, caused in part by time-varying atmospheric emission. For bright and localized sources such as planets and quasars we start the map-making process by utilizing a generic peak finding algorithm to mask the source in the timestreams; for other sources we produce a custom mask. After baseline corrections we compute the per-scan variance from the off source components of the timestreams. Finally, we project these timestreams to maps with a 2-D histogram where we estimate the flux per pixel with an inverse variance weighting of its constituents. Since each frequency channel has a different spectral response function and each detector has its own gain, this is done on a detector by detector basis.

### 3.1. Planet Calibration

The 32 feedhorn layout of the focal plane means that there are 32 separate lines of sight at any given time

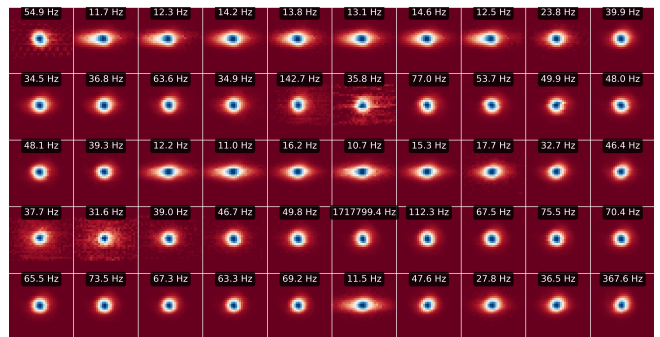


**Figure 2.** In each panel is a single detector image from a subset of detectors within a Jupiter observation which are normalized to a peak of one. Each image is  $4.2' \times 4.2'$ ; the mean beam size of TIME is  $30''$ , and Jupiter had an angular size of  $\sim 33''$  during these observations. The title of each panel is the time constant of each detector measured in Hz, demonstrating that the detectors with significant smearing are ones with slow time constants. However, the fitting methodology of convolving a 2-D Gaussian beam with a decaying exponential has poor performance when there is no smearing present in the image, hence the large spread in high time constant values. Detectors with slow time constants are discarded from this analysis.

in an observation that produce a  $\sim 13.5' \times 0.5'$  linear beam pattern. We describe here the process of aligning these different views with the operational pointing data from the ARO-12M by estimating the feedhorn pointing offsets.

We start the process of estimating these quantities by generating 2-D images of the planet, one per detector. From there we can fit a beam model, in this case a standard 2-D Gaussian convolved with a top hat disk kernel the angular size of the observed planet, and assess the pointing position of each feedhorn through the best-fit centers. We restrict our analysis to beams that measure a SNR  $> 10$ , a minimum amplitude of 20 arbitrary detector counts, have a beam profile that is greater than the diffraction limit, and where the ratio of the detector map RMS before and after subtracting the best fit beam model is  $< 0.8$ . These checks are necessary as we have groups of 32 detectors that share a common bias line and for these proto-type detectors it was not always possible to bias every detector within the superconducting transition region (V. L. Butler et al. 2026). Thus there are detectors that are not sensitive that may have weak signals due to inductive cross-talk with their neighbors. An example of a subset of the passing detectors from one observation are shown in Figure 2.

We then estimate the feedhorn offsets in two steps. First we take the best fit planet positions for each detector and compute the per-feedhorn mean. Then we compute the difference between each feedhorns mean position and feedhorn 8, which was aligned along the pointing of the telescope. As a follow-up we use these per-feedhorn pointing offsets to draw a mask of radius  $90''$  (approximately three times the expected beam-width) and reprocess the atmospheric removal. This is done as the first pass masks are sometimes imprecise, causing us to over-subtract our source. In this secondary processing step we also apply the relative feedhorn offsets to the detector TODs. Then, we re-fit Gaussian beams to these data and the same quality checks listed above are repeated. The new best fit centers can then be compared to an ephemeris position to obtain the absolute pointing offset.

All of the detector images that pass this second wave of quality checks are then used to estimate the per detector gain in a similar manner as described in S. F. Yang et al. (2026). Since these observations are of Jupiter, we use a Jupiter flux model, taken from ALMA’s calibration products (CASA Team et al. 2022), to compute a fiducial spectrum. In full detail, this is modeled by

$$I_\nu = B(\nu; T_b)\Omega\epsilon. \quad (2)$$

Above,  $\Omega$  is the angular size of Jupiter, which is estimated through JPL’s ephemeris (R. S. Park et al. 2021), and  $\epsilon$  is a coupling term between the primary beam of the 12M telescope and Jupiter’s semi-extended source structure. During these observations, Jupiter had an average angular size of  $\sim 33''$ , and we expect our beam FWHM to range in size from  $\sim 20''$  at 320 GHz to  $\sim 35''$  at 180 GHz, meaning that we cannot treat Jupiter as a point source. We thus include a model of the coupling,  $\epsilon$ , of a 2-D Gaussian beam centered on a uniform disk in our gain estimation;

$$\epsilon = \frac{1 - \exp(-x^2 \log 2)}{x^2 \log 2}, \quad (3)$$

where  $x$  is the ratio of the planet diameter to the beam FWHM. We then estimate the per detector gain by

$$G(\nu) = \frac{I_\nu}{A_c}. \quad (4)$$

Above,  $A_c$  is the best fit amplitude in arbitrary data counts. We note that because the atmospheric opacity is corrected in an earlier step this methodology is consistent with the description provided by S. F. Yang et al. (2026).

### 3.2. Applying Calibrations to OMC and G49.5

Before any steps to process science data are made we apply the gain corrections estimated in the previous step, and then produce maps following the methodology outlined in §3 and Figure 1, where a custom mask, shaped to the source’s extended signal, is utilized. As an additional step, we account for the uncertainty in the gain and atmospheric attenuation by adding these terms in quadrature with the per scan variance;

$$\sigma^2 = \gamma^2 \left( V + \frac{D^2}{G(\nu)^2} \sigma_G^2 + D^2 \sec^2(z) \sigma_\tau \right). \quad (5)$$

In this equation  $V$  is the estimated per-scan variance, in units of  $\text{Jy}^2$ , and  $D$  is the detector timestream in units of Jy. These data are then projected onto a map using the same inverse variance weighted 2-D histogram procedure described in §3.

#### 3.2.1. Quality Checks on OMC and G49.5 Images

Now that we have a set of calibrated maps of both OMC and G49.5 we go through another set of quality checks to keep high quality detectors. The first of these checks is to remove the edge channels. TIME was intentionally designed to have a pass band between two water vapor lines, where the lowest and highest frequency channels are explicitly observing the atmosphere. Thus

we limit our analysis to detectors within the pass-band of 200-300 GHz.

The second set of cuts is to remove detectors that have high time constants. As previously mentioned, the detectors used here have a response time that can cause images to blur along the scan direction. A clear example of this is shown in Figure 2, where some of those images are smeared along the scan direction (RA in this example) due to long time constants. The smearing is seen on either side of the planet because the 2-D raster scan strategy sweeps back and forth. These detectors are problematic because they cause a mis-estimate of flux. To determine which detectors have a slow time constant, we fit a Gaussian beam profile convolved with a decaying exponential. However, this fit is unstable. Thus to automate this pipeline for a large number of planet observations, we instead fit an elliptical beam profile and estimate the ellipticity. We find that an ellipticity value of  $< 0.3$  is sufficient to remove these slow detectors.

The final set of cuts are to cull detectors that are readout-noise dominated and show only white noise on faint sources, these detectors are thus a hindrance when integrating down the noise and we choose to filter them out. This is done by comparing each detector image to a spatial template of the source. This template is constructed by taking the average of all the remaining detector images divided by their peak flux (in the case of OMC this is the BN/KL region). We then compute a correlation coefficient between each detector image and this template image. Detectors that only show white noise will have a low correlation coefficient. We use a threshold of  $> 0.7$  to minimize the number of detectors cut from this process, while ensuring that we remove all of the readout dominated ones. After all of these cuts we then average across the feedhorn channels to create a set of spectral images.

#### 4. G49.5 OBSERVATIONS

G49 is a bright HII region in the Milky Way (J. M. Carpenter & D. B. Sanders 1998) and is a massive star forming complex that consists of multiple smaller clouds (W. Lim & J. M. De Buizer 2019). We observed one of the smaller clouds, G49.5, during the TIME 2022 commissioning run, and processed it according to the procedure outlined in §3. These observations are then compared to a BGPS measurement to demonstrate the accuracy of the gain calibration outlined in §3.1. This is done by computing a Bolocam broadband image which is the co-added flux of the TIME spectral images weighted by the Bolocam bandpass:

$$I_{BB}(x, y) = \sum_{\nu} I(\nu, x, y) T(\nu). \quad (6)$$

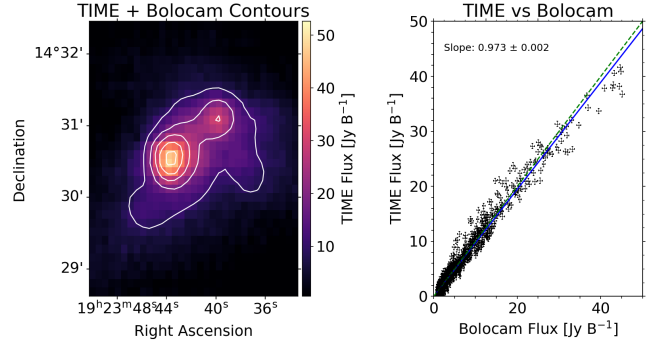


**Figure 3.** The left panel shows a broadband TIME image of G49.5, estimated by co-adding 42 spectral channels, of which 35 are measured with TIME and 7 are inferred from spectral index fits, weighted by the Bolocam bandpass. The white contours indicate the relative position of Bolocam demonstrating that the astrometry of both data sets is aligned. On the right is a plot of the per pixel flux density of TIME versus Bolocam. The blue line is a line of best fit, with best fit slope of 0.973 indicating a  $< 3\%$  agreement in flux calibration.

Above,  $x$  and  $y$  give the image coordinates,  $I_{BB}$  represents the broadband image, and  $T(\nu)$  represents the Bolocam bandpass. To ensure that we are not underestimating the flux when comparing to Bolocam, we need an estimate of the flux from the missing spectral channels. To do this we fit a power law to each pixel while masking channels between 210 – 235 GHz and 254 – 277 GHz to remove bias from bright emission lines. We then compute the posterior predictive of these fits and use them to fill in the missing spectral channels. In Figure 3 we show the resulting broadband TIME image with Bolocam contours overlaid. We then do a pixel-pixel comparison with Bolocam and fit a zero-offset line as an estimate of the average ratio of TIME to Bolocam flux, which is shown in the right panel of Figure 3. We estimate a  $0.973^{+0.002}_{-0.002}$  agreement indicating that the flux calibration is consistent with Bolocam to within  $< 3\%$ .

#### 5. OMC

We have also processed observations of the OMC complex which was observed at least once per day through the 2022 winter commissioning. There are a total of 13 separate OMC observations that are processed using the procedure described in §3.

We produce a spectrum of OMC BN/KL. This analysis is done in a set of four steps. In the first we average each observation together by frequency and then jointly fit two rotated and elliptical gaussian models to both the northern and southern compact regions at each frequency. We then take the median best fit centers and median best fit angular sizes and use those as constraints

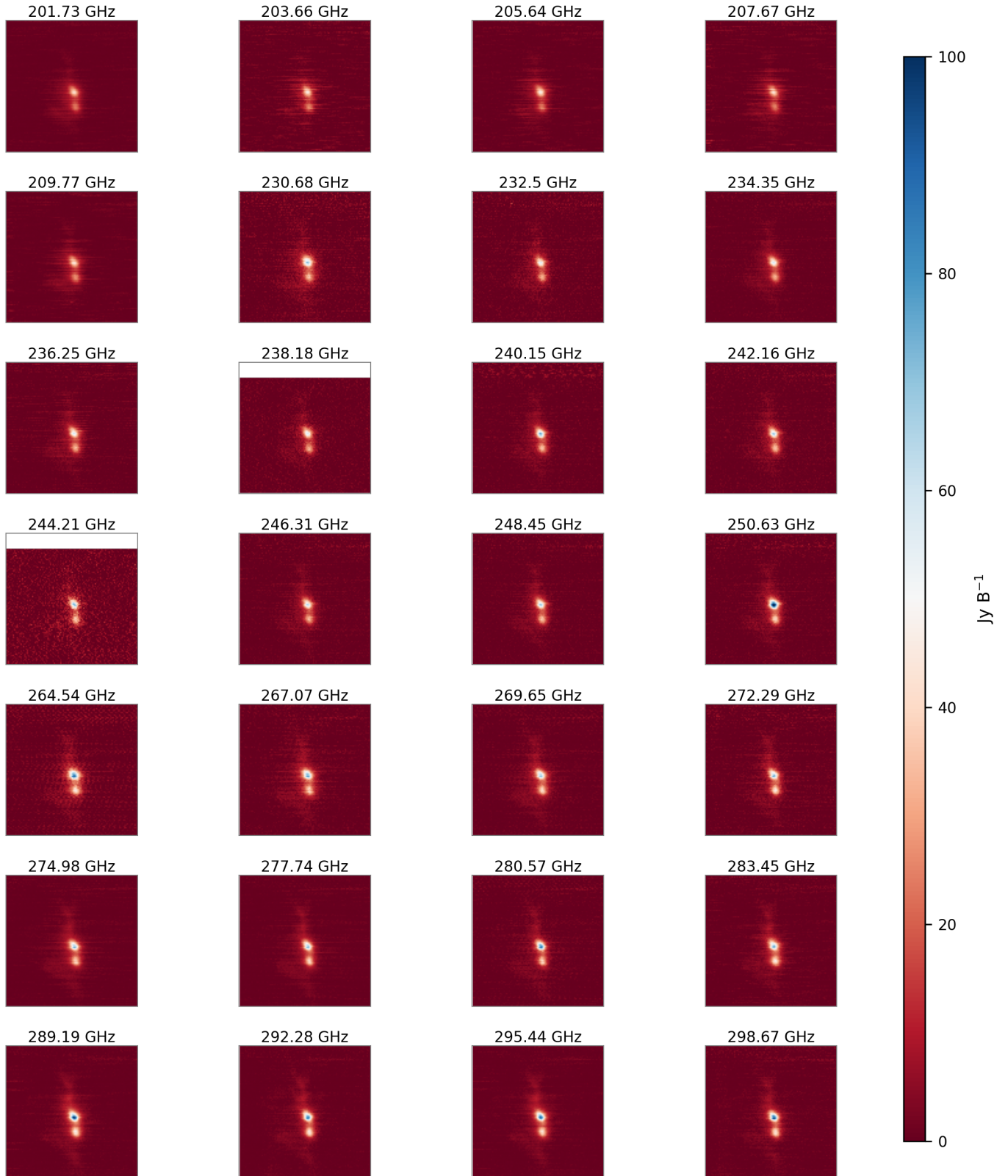


**Figure 4.** The spectral images of OMC after we have averaged across a sub-set of OMC observations that were taken at higher spatial resolution as denoted in Table 1.

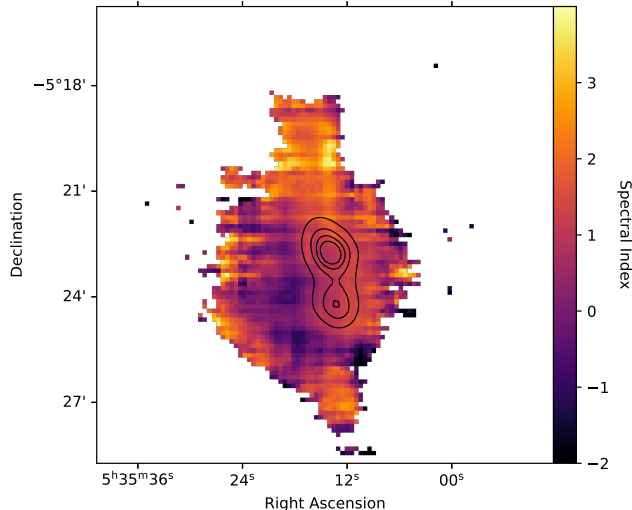


**Figure 5.** A spectral index map of OMC, with a contour of the TIME broadband image overlaid, highlighting the two compact regions. The spectral index of the BN/KL region is 2 which is consistent with the expectation for a star forming region, and other measurements (F.-X. Désert et al. 2025)

in a second re-fit of the data. This is done as in some spectral channels the extended emission can confuse the fitting process and lead to under-fitting of the compact regions. From this second pass of fits we generate another set of median best fit centers and angular sizes. This time we hold these constants per frequency and fit for the flux from individual detectors per observation. Within an observation detectors are then averaged together by frequency producing the spectra in Figure 6

We also generate a map of the spectral indices. To do this we average these observations together by frequency and fit a power law to each pixel of the image. Frequencies in the range of 210–235 GHz and 254–277 GHz are masked so that we do not bias these fits with spectral line emission. The resulting spectral index map is shown in Figure 5.

## 6. DISCUSSION

We now discuss some lessons learned and improvements that could be made to the TIME instrument for upcoming observing runs. Inhomogeneities inherent in the small-scale detector fabrication associated with a pathfinder instrument on the scale of TIME, will require particular care in future observing operations. All else being equal, achieved on-sky detector gains will change with both atmospheric loading and the thermal bath temperature of the focal plane, both disturbing the overall thermoelectric feedback loop that governs the equilibrium state of the TES and altering the responsivity of the detector.

In future observing runs we will use proportional/integral/derivative (PID) loop to stabilize the stage temperature and remove this contribution to bias point drift that may affect gains and yield. This system was prototyped during the 2022 commissioning observations, but due to temperature instabilities from aging equipment it reduced the amount of observing time available each day and we thus decided to turn it off. These old parts are currently being refurbished and we anticipate in future observing seasons we will be able to consistently PID the focal plane and reduce the effect of thermal drifts on gain sensitivity, which is crucial to probing the faint LIM signals we are interested in observing.

We are also working towards building detectors that can be more stably biased at a common set point (V. L. Butler et al. 2026). Beyond that, we now have many more detector modules than in 2022. The modular nature of the focal plane allows us to better place these modules in a way that maximizes on-sky yield.

With the opacity at Kitt Peak being fairly high ( $\tau \approx 0.1$  at zenith in top 10% conditions), real-time monitoring of the atmosphere is more important than at other high and dry sites. During the 2022 run the dedicated water vapor radiometer at the ARO facility was non-operational, forcing us to rely purely on atmospheric forecasting models. However, for our subsequent 2026 engineering run this radiometer was operational alongside a newly developed weather station. We are investigating the possible long-term use of this weather station alongside global navigation satellite system signals for high-fidelity, cost-effective estimates of precipitable water vapor content (Zemcov et al., in prep; see also previous work by W. M. Wood-Vasey et al. (2022); J. Sugiyama et al. (2024)). In addition to these improvements of opacity monitoring on the site, we will be making empirical measurements of the atmosphere during our scientific observing runs.

### 6.1. Expectations for Future TIME Sensitivities

We estimate the aggregate sensitivity of the TIME instrument to inform future scientific deployments. This quantity is derived directly from the per-scan variance of each detector in each observation. Subsequent scans in the same observation are averaged together, we then further average observations together on a per-detector basis. Due to the prototype nature of the 2022 observing run, we use the top performing detectors as a measure of the achievable sensitivities with a more developed instrument. These values are  $300 \text{ mJy s}^{1/2}$  or  $10 \text{ MJy sr}^{-1} \text{ s}^{-1}$  per detector. Simulations from G. Sun et al. (2021) estimate the constraining power we

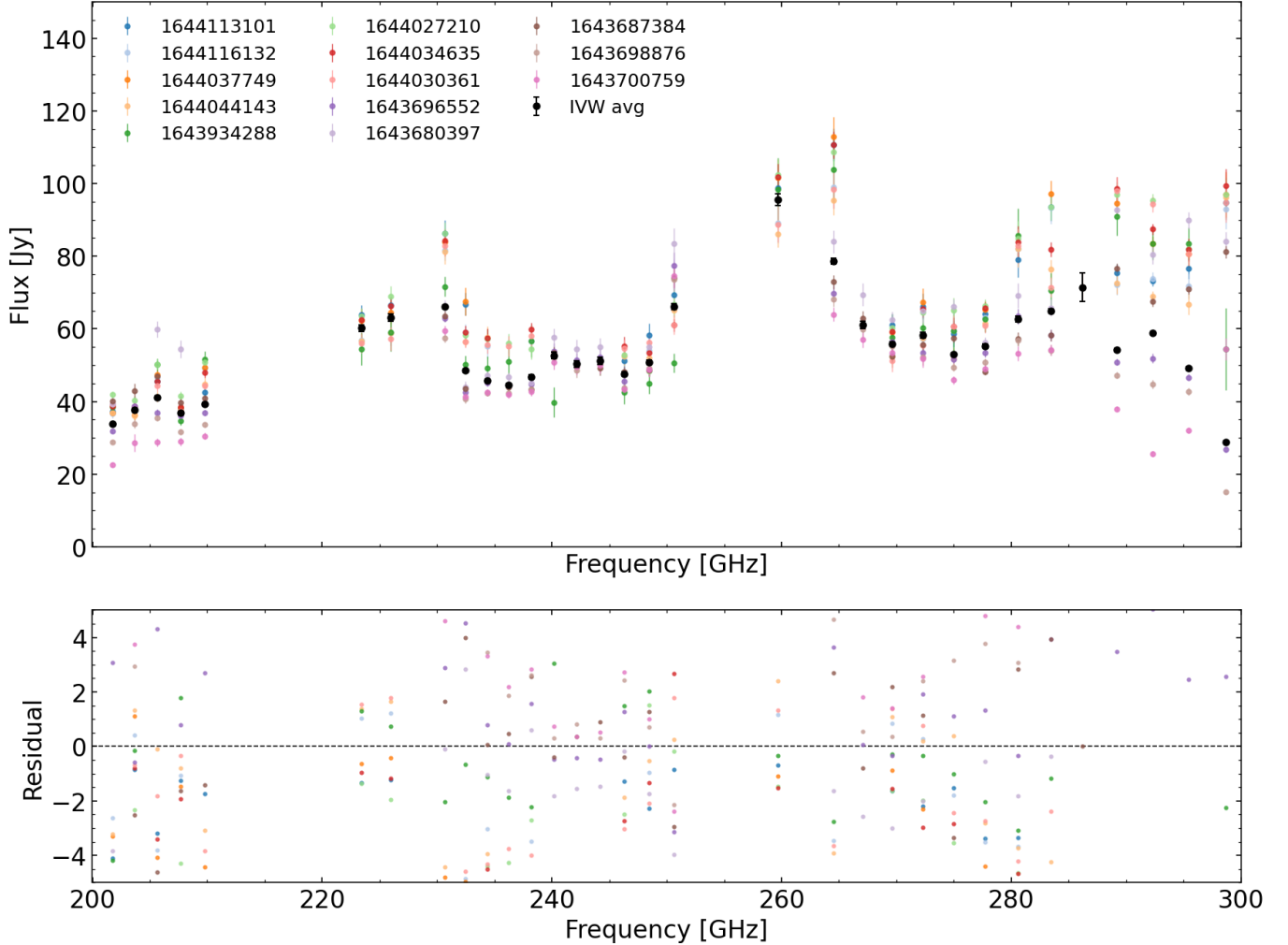


**Figure 6.** Spectra of the BN/KL region of OMC. Different observations are recorded in different colors with the inverse variance weighted average of these observations in black. In the bottom panel a residual plot is shown where we estimate the difference between each observation and the averaged spectrum in units of uncertainty. This demonstrates that with accurate estimates of opacity (i.e. in the low frequency range) we are able to produce calibrated images of sources, where subsequent measurements of the same source can properly be integrated down to reduce random noise.

**Table 2.** Sensitivity and Mapping Speed Estimates

target signal	LIM field	SZe	Pre-Stellar Core
Required Field Size	$1.3^\circ \times 0.007^\circ$	$0.23^\circ \times 0.08^\circ$	$0.23^\circ \times 0.08^\circ$
Desired Sensitivity	$0.02 \text{ MJy sr}^{-1}$	$0.04 \text{ MJy sr}^{-1}$	50 mJy
Hours Required	403	208	3

NOTE—TIME is designed to observe a 1-D patch of sky. As such, we demonstrate the total number of observing time needed to integrate down a  $1.3^\circ$  line (as simulated in [G. Sun et al. \(2021\)](#)) to reach a sensitivity of  $0.02 \text{ MJy sr}^{-1}$  ([D. T. Chung et al. 2020](#)) is 403 hours.

can achieve on different [CII] and CO power spectra observables assuming a noise equivalent intensity of  $5 \text{ MJy sr}^{-1} \text{ s}^{-1}$ . Thus demonstrating that a more mature instrument will be capable of measuring LIM signals. This sensitivity would also allow us to access small surveys to perform additional science cases such as the SZ effect in galaxy clusters, pre-stellar cores, and planetary nebulae in hundreds of hours of integration time.

We have built a raw data processing pipeline that produces calibrated spectral images of any science target with TIME. This pipeline was then used to produce spectral images of OMC and G49.5. Then, we assessed the relative calibration of TIME to another instrument and to itself with subsequent observations. Based on these outcomes we have demonstrated a preliminary performance of the TIME instrument and outlined a path forward for improving instrument performance.

## 7. ACKNOWLEDGMENTS

This material is based upon work supported by the National Science Foundation under Grant Nos. 1602677,

1653228, 1910598, 2308039, 2308040, 2308041, and 2308042.

The TIME collaboration acknowledges the critical contributions of the Arizona Radio Observatory engineers and operators, including Kevin Bays, Tom Folkers, Natalie Gandilo, Blythe Guvenen, Sean Keel, and Martin McColl. We also acknowledge Sukhman Singh and Ibrahim Shehzad at Cornell and Lisa Nasu-Yu at the University of Toronto for early contributions to data analysis, observations, and simulations that ultimately informed this work.

ATC acknowledges support as a Fred Young Faculty Fellow at Cornell University.

DTC was supported by a CITA/Dunlap Institute postdoctoral fellowship for much of this work. The Dunlap Institute is funded through an endowment established by the David Dunlap family and the University of Toronto. Research in Canada is supported by NSERC and CIFAR.

## REFERENCES

- Aguirre, J. E., Ginsburg, A. G., Dunham, M. K., et al. 2011, *ApJS*, 192, 4, doi: [10.1088/0067-0049/192/1/4](https://doi.org/10.1088/0067-0049/192/1/4)
- Bally, J. 2008, in *Handbook of Star Forming Regions*, Volume I, ed. B. Reipurth, Vol. 4, 459, doi: [10.48550/arXiv.0812.0046](https://doi.org/10.48550/arXiv.0812.0046)
- Battistelli, E. S., Amiri, M., Burger, B., et al. 2008, *Journal of Low Temperature Physics*, 151, 908, doi: [10.1007/s10909-008-9772-z](https://doi.org/10.1007/s10909-008-9772-z)
- Butler, V. L., Crites, A. T., Berek, S., et al. 2024, in *Millimeter, Submillimeter, and Far-Infrared Detectors and Instrumentation for Astronomy XII*, ed. J. Zmuidzinas & J.-R. Gao, Vol. 13102, *International Society for Optics and Photonics (SPIE)*, 131022G, doi: [10.1117/12.3021442](https://doi.org/10.1117/12.3021442)
- Butler, V. L., Bock, J. J., Chung, D. T., et al. 2026, *IEEE Transactions on Applied Superconductivity*, 36, 2103507, doi: [10.1109/TASC.2026.3694584](https://doi.org/10.1109/TASC.2026.3694584)
- Carpenter, J. M., & Sanders, D. B. 1998, *AJ*, 116, 1856, doi: [10.1086/300534](https://doi.org/10.1086/300534)
- CASA Team, Bean, B., Bhatnagar, S., et al. 2022, *PASP*, 134, 114501, doi: [10.1088/1538-3873/ac9642](https://doi.org/10.1088/1538-3873/ac9642)
- Chung, D. T., Viero, M. P., Church, S. E., & Wechsler, R. H. 2020, *ApJ*, 892, 51, doi: [10.3847/1538-4357/ab798f](https://doi.org/10.3847/1538-4357/ab798f)
- Crites, A. T., Bock, J. J., Bradford, C. M., et al. 2014, in *Society of Photo-Optical Instrumentation Engineers (SPIE) Conference Series*, Vol. 9153, *Millimeter, Submillimeter, and Far-Infrared Detectors and Instrumentation for Astronomy VII*, ed. W. S. Holland & J. Zmuidzinas, 91531W, doi: [10.1117/12.2057207](https://doi.org/10.1117/12.2057207)
- Désert, F.-X., Macías-Pérez, J. F., Beelen, A., et al. 2025, *A&A*, 701, A210, doi: [10.1051/0004-6361/202555320](https://doi.org/10.1051/0004-6361/202555320)
- Fujita, S., Torii, K., Kuno, N., et al. 2021, *PASJ*, 73, S172, doi: [10.1093/pasj/psz028](https://doi.org/10.1093/pasj/psz028)
- Hunacek, J. 2020, PhD thesis, California Institute of Technology, Division of Physics, Mathematics and Astronomy
- Hunacek, J., Bock, J., Bradford, C. M., et al. 2018, *Journal of Low Temperature Physics*, 193, 893, doi: [10.1007/s10909-018-1906-3](https://doi.org/10.1007/s10909-018-1906-3)
- Kovetz, E., Breyse, P. C., Lidz, A., et al. 2019, *BAAS*, 51, 101, doi: [10.48550/arXiv.1903.04496](https://doi.org/10.48550/arXiv.1903.04496)
- Li, C.-T., Bradford, C. M., Crites, A., et al. 2018, in *Millimeter, Submillimeter, and Far-Infrared Detectors and Instrumentation for Astronomy IX*, ed. J. Zmuidzinas & J.-R. Gao, Vol. 10708, *International Society for Optics and Photonics (SPIE)*, 107083F, doi: [10.1117/12.2311415](https://doi.org/10.1117/12.2311415)
- Lim, W., & De Buizer, J. M. 2019, *ApJ*, 873, 51, doi: [10.3847/1538-4357/ab0288](https://doi.org/10.3847/1538-4357/ab0288)

- Mayer, E. C., Lowe, I. N., Marrone, D. P., et al. 2025, arXiv e-prints, arXiv:2511.09446, doi: [10.48550/arXiv.2511.09446](https://doi.org/10.48550/arXiv.2511.09446)
- Paine, S. 2022, am: Microwave through submillimeter-wave propagation tool for the terrestrial atmosphere,, Astrophysics Source Code Library, record ascl:2205.002 <http://ascl.net/2205.002>
- Park, R. S., Folkner, W. M., Williams, J. G., & Boggs, D. H. 2021, AJ, 161, 105, doi: [10.3847/1538-3881/abd414](https://doi.org/10.3847/1538-3881/abd414)
- Sayers, J., Golwala, S. R., Ade, P. A. R., et al. 2010, ApJ, 708, 1674, doi: [10.1088/0004-637X/708/2/1674](https://doi.org/10.1088/0004-637X/708/2/1674)
- Sugiyama, J., Nishino, H., & Kusaka, A. 2024, MNRAS, 528, 4582, doi: [10.1093/mnras/stae270](https://doi.org/10.1093/mnras/stae270)
- Sun, G., Chang, T.-C., Uzgil, B. D., et al. 2021, ApJ, 915, 33, doi: [10.3847/1538-4357/abfe62](https://doi.org/10.3847/1538-4357/abfe62)
- Wilson, B. A., Dame, T. M., Masheder, M. R. W., & Thaddeus, P. 2005, A&A, 430, 523, doi: [10.1051/0004-6361:20035943](https://doi.org/10.1051/0004-6361:20035943)
- Wood-Vasey, W. M., Perrefort, D., & Baker, A. D. 2022, AJ, 163, 283, doi: [10.3847/1538-3881/ac63bb](https://doi.org/10.3847/1538-3881/ac63bb)
- Yang, S. F., McAtee, S. M., Vaughan, B. J., et al. 2026, ApJ, 1003, 23, doi: [10.3847/1538-4357/ae606c](https://doi.org/10.3847/1538-4357/ae606c)